PHYSICAL REVIEW A **84**, 023832 (2011)

High-energy-throughput pulse compression by off-axis group-delay compensation in a laser-induced filament

A. A. Voronin,[1] S. Ališauskas,[2] O. D. Mücke,[2] A. Pugžlys,[2] A. Baltuška,[2] and A. M. Zheltikov[1,3,*]
[1] *Physics Department, International Laser Center, M. V. Lomonosov Moscow State University, Moscow 119992, Russia*
[2] *Photonics Institute, Vienna University of Technology, Gusshausstrasse 27-387, 1040 Vienna, Austria*
[3] *Department of Physics and Astronomy, Texas A&M University, College Station, Texas 77843-3257, USA*
(Received 17 January 2011; published 18 August 2011)

Off-axial beam dynamics of ultrashort laser pulses in a filament enable a radical energy-throughput improvement for filamentation-assisted pulse compression. We identify regimes where a weakly diverging wave, produced on the trailing edge of the pulse, catches up with a strongly diverging component, arising in the central part of the pulse, allowing sub-100-fs millijoule infrared laser pulses to be compressed to 20–25-fs pulse widths with energy throughputs in excess of 70%. Theoretical predictions have been verified by experimental results on filamentation-assisted compression of 70-fs, 1.5-μm laser pulses in high-pressure argon.

DOI: 10.1103/PhysRevA.84.023832 PACS number(s): 42.65.Re, 42.65.Jx, 42.65.Sf

Filamentation of ultrashort laser pulses [1–3] is one of the most exciting recent discoveries in optical physics. As a physical phenomenon, it involves complex, strongly coupled spatiotemporal dynamics of optical field wave forms in nonlinear, fast-ionizing media, giving rise to unique regimes of ultrafast electrodynamics [4–7]. This regime of short-pulse propagation offers promising solutions for long-range electromagnetic radiation energy transfer [8] and remote sensing of the atmosphere [9]. In ultrafast optical science, laser filamentation finds growing applications as a powerful technique of pulse compression [10–14], enabling the generation of high-peak-power carrier-envelope-phase (CEP) stable few-cycle optical field wave forms within a broad frequency range from the deep ultraviolet [15,16] to the near- and midinfrared [17–19].

The key limitation of the filamentation-based pulse compression technology is related to a strong spatial chirp acquired by a laser beam in the course of filamentation [2,3]. As a consequence, spatial filtering with a diaphragm is typically needed for the selection of the paraxial part of the beam, providing the highest efficiency of pulse compression. This beam aperturing dramatically reduces the energy of compressed light pulses, lowering energy conversion from the input pulse to the compressed output. Here, we identify a promising scenario of filamentation-assisted pulse compression where a compensation of the group delay between a weakly diverging section of a laser beam on the trailing edge of the pulse and a strongly diverging beam section in the central part of the pulse enables a high-energy-throughput compression of ultrashort laser pulses.

We analyze the spatiotemporal filamentation dynamics of ultrashort laser pulses by numerically solving the field evolution equation using the framework of the slowly evolving wave approximation (SEWA) [20] modified [21,22] to include ionization effects:

$$\frac{\partial}{\partial z}A(\omega,r,z)=\left[\frac{ic}{2\omega}\Delta_{\perp}+i\hat{D}(\omega)\right]A(\omega,r,z)+ \\ +\hat{F}\left\{\left[i\frac{n_2\omega_0}{c}\hat{T}I-i\frac{\omega_0}{2c\rho_c\hat{T}}\rho \right.\right. \\ \left.\left.-\frac{(\rho_0-\rho)U_iW}{2I}-\frac{\sigma}{2}\rho\right]A(\eta,r,z)\right\}. \quad (1)$$

Here, $A(\eta,r,z)$ is the complex field amplitude, $A(\omega,r,z)$ is its Fourier transform, $I=|A(\eta,r,z)|^2$ is the field intensity, z is the coordinate along the propagation path, $\eta=t-z/u$ is the time in the retarded frame of reference, t is the time in the laboratory frame of reference, u is the group velocity, r is the radial coordinate, $\omega=2\pi c/\lambda$ is the frequency of the field with the wavelength λ, $\Delta_{\perp}=r^{-1}\partial(r\partial/\partial r)/\partial r$ is the diffraction operator, $\hat{D}=\beta(\omega)-\beta(\omega_0)-(\omega-\omega_0)\partial\beta/\partial\omega|_{\omega_0}$ is the dispersion operator, ω_0 is the central frequency of the input laser field, $\beta(\omega)=\omega n(\omega)/c$ is the propagation constant, $n(\omega)$ is the refractive index of the gas, $\hat{F}$ is the Fourier transform operator, n_2 is the nonlinear refractive index coefficient, c is the speed of light in vacuum, $\hat{T}=1+i\omega_0^{-1}\partial/\partial\eta$, ρ is the electron density, ρ_0 is the initial density of neutral atoms, U_i is the ionization potential, W is the ionization rate, σ is the impact ionization cross section, $\rho_c=\omega_0^2 m_e\varepsilon_0/e^2$ is the critical plasma density, m_e and e are the electron mass and charge, and ε_0 is vacuum permittivity.

The pulse propagation equation (1) is solved jointly with the equation for the electron density: $\partial\rho/\partial\eta=W(\rho_0-\rho)+\sigma\rho I/U_i$. The ionization rate W is calculated using the Popov-Perelomov-Terentyev modification [23] of the Keldysh formula [24]. The impact ionization cross section σ is included in the model through the Drude formula $\sigma(\omega)=e^2\tau_c[m_e\varepsilon_0 c(1+\omega^2\tau_c^2)]^{-1}$, where τ_c is the electron collision time. Our numerical algorithm is based on the split-step method, with a quasifast Hankel transform used to calculate the diffraction operator and the fifth-order Runge-Kutta method solving the equation for the electron density. The time discretization step was 0.34 fs. The discretization step in the radial coordinate was varied, with its minimum value near

---

[*] zheltikov@phys.msu.ru

the filament axis being equal to 1.5 μm. The step along the z axis was varied in such a way as to keep the nonlinear phase shift in each step below 0.05. The overall number of computation nodes was equal to 2^{15} along the radial coordinate and 2^{13} along the time axis. The model was implemented in parallel codes, which were run on the Intel Xeon E5472 3.0-GHz supercomputer. This grid, known from the earlier work on short-pulse filamentation [18], has been chosen to allow for the visualization of fine details of pulse filamentation dynamics. With an appropriate grid optimization, however, it was possible to substantially speed up simulations for the conditions considered here without sacrificing any of the critical details of pulse propagation dynamics.

Our simulations were intended to model and understand filamentation-assisted pulse compression experiments [17], where 70-fs, 2.2-mJ light pulses with a central wavelength of 1.57 μm, delivered by an infrared optical parametric chirped pulse amplifier (OPCPA), were compressed to pulses with a pulse width of ~20 fs and an energy of 1.5 mJ through filamentation in argon at a pressure of

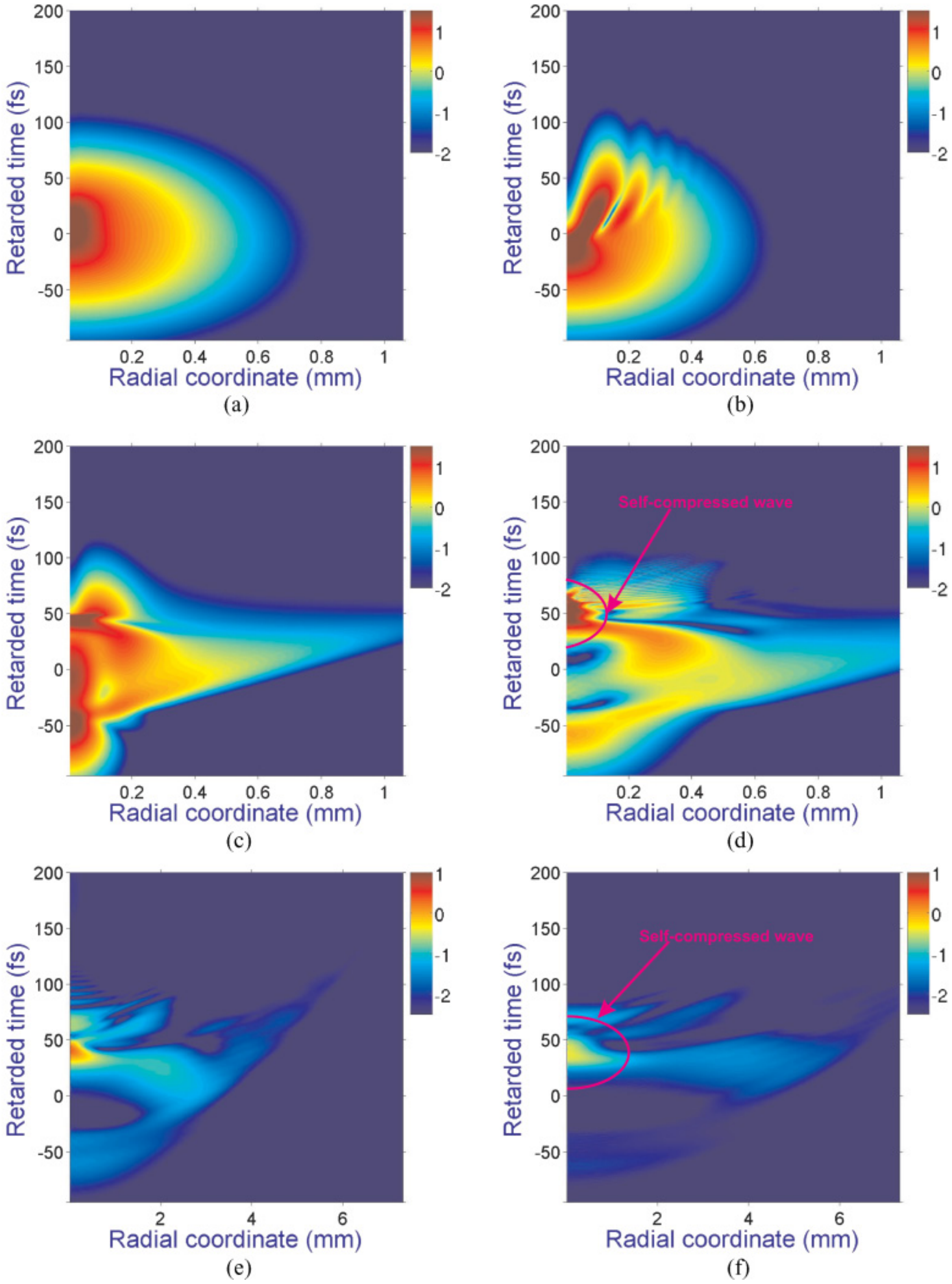

FIG. 1. (Color online) Spatiotemporal maps of the field intensity (the color encodes the logarithm of the field intensity) in a laser pulse with $\tau_0 = 70$ fs, $E_0 = 2.2$ mJ, and $\lambda_0 = 1565$ nm propagating in argon at $p = 5$ bars: (a) $z = 40.4$ cm, (b) 42.2 cm, (c) 50.1 cm, (d) 55.0 cm, (e) 101.0 cm, and (f) 145.0 cm.

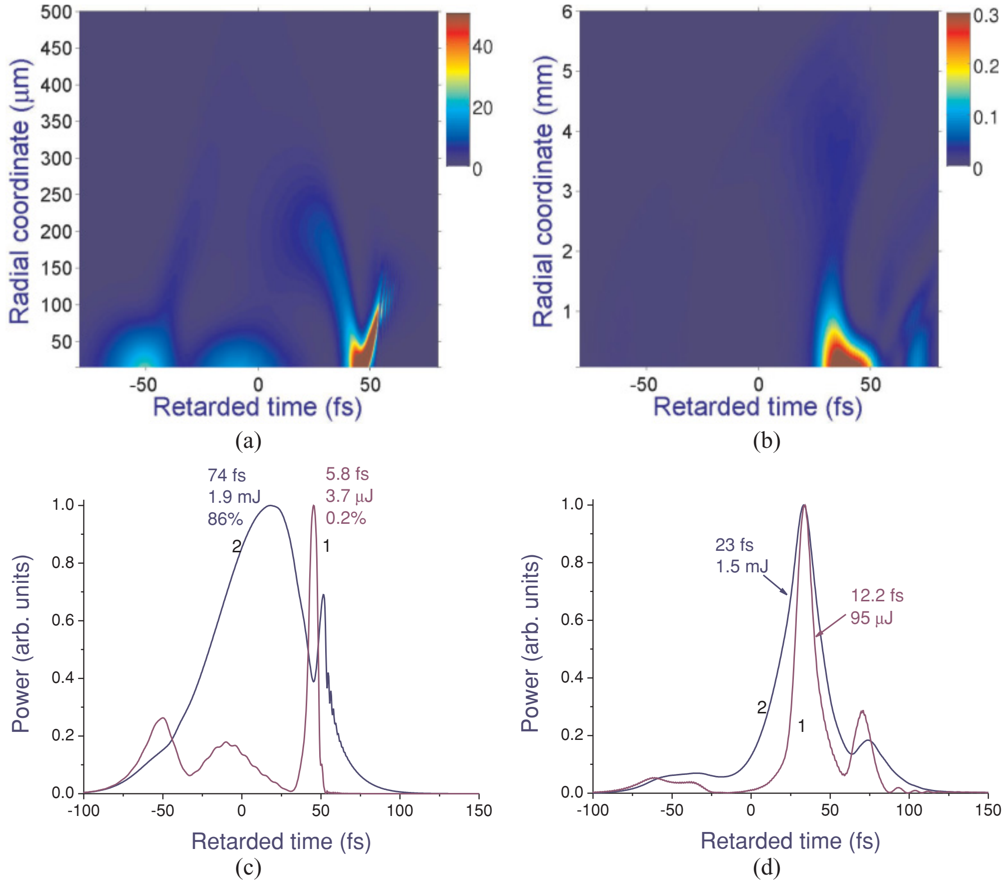

(a) (b) (c) (d)

FIG. 2. (Color online) (a), (b) Spatiotemporal maps and (c), (d) temporal envelopes of the field intensity (the color in panels (a) and (b) encodes the field intensity on the linear scale) in a laser pulse with $\tau_0 = 70$ fs, $E_0 = 2.2$ mJ, and $\lambda_0 = 1565$ nm propagating in argon at $p =$ 5 bars: (a) $z = 52$ cm and (b) 145 cm. (c), (d) Temporal envelopes of laser pulses filtered by a pinhole with a diameter of (c) 25 μm (curve 1) and 12 mm (curve 2) and (d) 2 mm (1) and 12 mm (2) placed at (c) $z = 52$ cm and (d) 145 cm.

5 bars. To mimic conditions of these experiments, we set $\lambda_0 = 2\pi c/\omega_0 = 1565$ nm, $n_2 = 1.1\times10^{-19}(p/p_{\text{atm}})$ cm^2/W [25], and $\rho_0 = 2.7 \times 10^{19}(p/p_{\text{atm}})$ cm^{-3}, where p is the gas (argon) pressure and p_{atm} is the atmospheric pressure. The ionization potential of argon is $U_i = 15.76$ eV. The time constant in the Drude model is taken equal to $\tau_c = 190 \cdot (p_{\text{atm}}/p)$ fs. Dispersion of argon was included through the Sellmeier equation [26]. We assume a Gaussian input laser pulse with an FWHM pulse width $\tau_0 = 70$ fs, pulse energy $E_0 = 2.2$ mJ, beam radius $w = 1.5$ mm, and wave-front curvature $f = 50$ cm.

The spatiotemporal dynamics of an ultrashort laser pulse with the previously specified parameters in high-pressure argon are illustrated in Figs. 1(a)–1(f). Behind the nonlinear focus ($z_f = 42$ cm for the chosen parameters), the trailing edge of the pulse experiences strong defocusing [Fig. 1(b)] due to a negative lens created by the spatial profile of the electron density induced by the central, most powerful part of the laser pulse, as well as its leading edge. Around $z = 50$ cm, a secondary focus arises on the trailing edge of the pulse as a part of the standard short-pulse filamentation scenario [2,3,18,27]. This refocusing gives rise to an intense self-compressed wave, which is confined both spatially and temporally near the beam axis on the back of the pulse [Figs. 1(d), 2(a), and 2(b)]. The spatial divergence of this part of the beam is suppressed by the joint effect of Kerr and plasma nonlinearities, making this wave channel along the axis of the filament [Figs. 2(a) and 2(b)]. In spite of its high intensity, reaching 90 TW/cm^2 at $z = 52$ cm in the regime considered here, this self-compressed wave carries only a small fraction of the total laser field energy [Figs. 2(c) and 2(d)]. Spatial filtering of the self-compressed wave using a diaphragm with a pinhole diameter of 25 μm will thus yield an ultrashort pulse [curve 1 in Fig. 2(c)] with a pulse width of 5.8 fs, corresponding to 1.1 field cycle, and an energy of 3.7 μJ, corresponding to energy conversion from the input field to the compressed pulse output with an efficiency of only 0.2%. A pinhole with a diameter of 200 μm would transmit a pulse with a pulse width of 6.1 fs and an energy of 127 μJ, corresponding to an energy conversion efficiency of 5.8%. For comparison, we also present in Fig. 2(c) (curve 2) a temporal envelope of a pulse filtered by a pinhole with a diameter of 12 mm. The energy of the pulse transmitted through such a pinhole is 1.9 mJ (86% of the entire output energy), but its pulse width (74 fs) is longer than the input pulse width.

We will now demonstrate that the input-to-compressed output energy conversion efficiency can be radically improved using the properties of beam dynamics inherent in an ultrashort laser pulse in the filamentation regime. The general tendencies of these dynamics are illustrated in Figs. 3 and 4, presenting the spatiotemporal maps of ultrashort light pulses in the

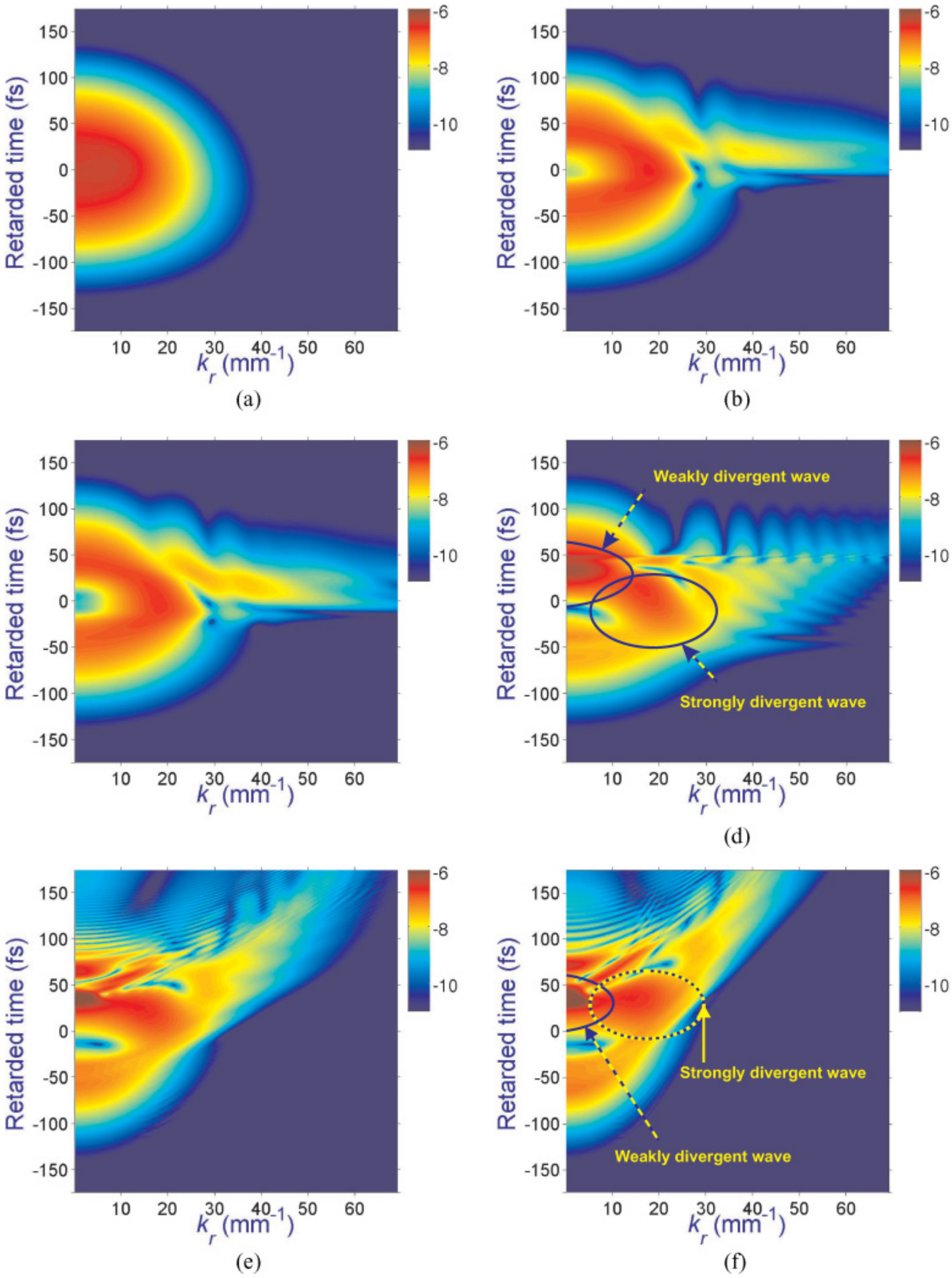

(a) (b)

(d)

(e) (f)

FIG. 3. (Color online) The $\eta - k_r$ maps of the field intensity (the color encodes the logarithm of the field intensity) in a laser pulse with $\tau_0 = 70$ fs, $E_0 = 2.2$ mJ, and $\lambda_0 = 1565$ nm propagating in argon at $p = 5$ bars: (a) $z = 35.1$ cm, (b) 42.8 cm, (c) 47.1 cm, (d) 50.1 cm, (e) 101.0 cm, and (f) 145.0 cm.

filamentation regime on the $\eta - k_r$ plane, k_r being the transverse part of the wave vector k. As can be seen from these maps, the spatiotemporal dynamics of an ultrashort laser pulse behind the nonlinear focus in a filament involve sectioning of a beam into a strongly diverging part, corresponding to the central part of the pulse, and a weakly diverging component in the trailing edge of the pulse. Around $z = 50$ cm [Fig. 3(d)], the strongly diverging wave is confined to a central section of the laser pulse approximately between -20 and $+20$ fs. The energy of this component is estimated as 0.86 mJ. The weakly diverging part of the field is localized between 20 and 50 fs [Fig. 3(d)], its energy estimated as 0.55 mJ. To quantify the difference in the divergence of these two components, we introduce an angle α between beam trajectories 1 and 2 representing these components and the z axis [Fig. 4(a)]. At $z_{\mathrm{nf}} \approx 50$ cm [Figs. 3(d) and 4(b)], i.e., right behind the nonlinear focus, this angle is $\alpha \approx 0.0043$ rad. The group delay between the weakly and strongly diverging waves at $z_{\mathrm{nf}} = 50$ cm is $\Delta\tau \approx 30$ fs [Fig. 4(b)]. As the weakly diverging component on the back of the pulse has a larger projection of its velocity on the z axis, it tends to catch up with the strongly divergent wave as a part of filamentation dynamics. For laser

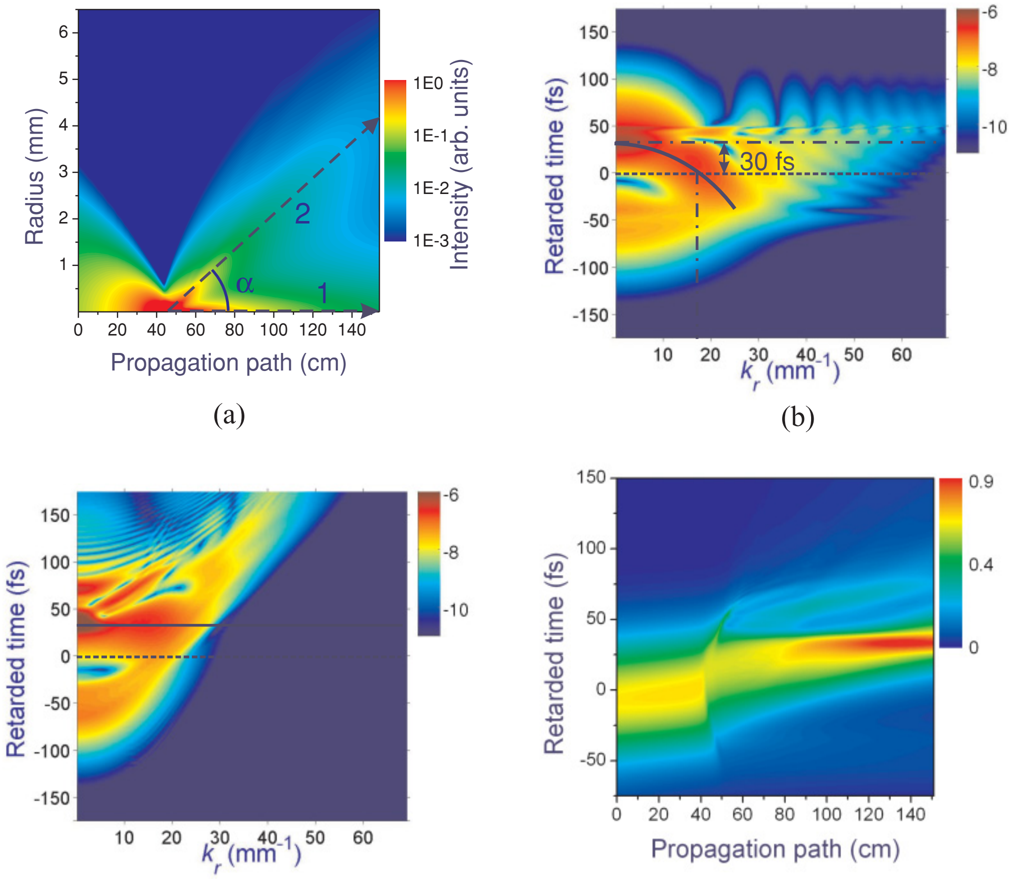

(a) (b) (c) (d)

FIG. 4. (Color online) (a) Dynamics of the laser beam in the filament. The compressed solitary wave forming on the trailing edge of the pulse propagates along the z axis (beam trajectory 1), while the diverging part of the beam propagates along beam trajectory 2, making an angle α with beam trajectory 1. (b), (c) The $\eta-k_r$ maps of the field intensity (on the logarithmic scale) at (b) $z = 50$ cm and (c) 145 cm. The dashed horizontal line shows time zero, corresponding to the center of the input pulse in the retarded frame of reference. (d) Evolution of the field intensity integrated over the beam. The input pulse parameters and gas pressure are as specified in Fig. 1.

pulses with the previously specified parameters, the weakly diverging component becomes synchronized with the strongly divergent wave at $z \approx 145$ cm [Figs. 3(f) and 4(c)].

Although the propagation of both components in the ionized gas is essentially nonlinear, useful insights into this regime of filamentation-assisted pulse compression can be gained by using a rough approximation of a linear, vacuumlike propagation of beam components. Assuming that these components propagate exactly along beam trajectories 1 and 2 at the speed of light in vacuum c, we find that the weakly diverging component will catch up with the strongly diverging wave at a distance $z_0 \approx 2\Delta\tau c\alpha^{-2} + z_{\mathrm{nf}}$. With $\Delta\tau \approx 30$ fs, $\alpha \approx 0.0043$ rad, and $z_{\mathrm{nf}} \approx 50$ cm, we find $z_0 \approx 145$ cm. This simple, zeroth-order estimate provides a surprisingly accurate prediction for the propagation path where the weakly diverging component becomes synchronized in time with the diverging wave [Figs. 3(f) and 4(c)]. On a spatiotemporal map showing the field intensity integrated over the beam as a function of the retarded time and the propagation path [Fig. 4(d)], this type of pulse evolution scenario is represented by a time profile that displays a gradual compression from $z_{\mathrm{nf}} \approx 50$ cm to $z \approx 145$ cm. These dynamics yield a pulse with an FWHM pulse width of 23 fs (Fig. 5(a)) and an energy of 1.5 mJ at the output of the filament ($z \approx 145$ cm), corresponding to an input-to-compressed-output energy conversion efficiency of ∼70%.

In Figs. 5(a) and 5(b), we compare predictions of our simulations with the results of experimental studies [17] of filamentation in argon at a pressure of 5 bars induced by 70-fs, 2.2-mJ light pulses with a central wavelength of 1.57 μm, delivered by an IR OPCPA, consisting of a diode-pumped solid-state Yb: KGW (potassium gadolinium tungstate) master-oscillator power amplifier and four stages of carrier-envelope-phase-stable parametric amplification. No beam aperturing was used in experiments, with a compressed pulse behind the filament having an FWHM width of ∼20 fs and an energy of 1.5 mJ. Because of the low beam divergence of the compressed filament output, no additional measures were needed to collimate radiation before pulse characterization. Typical measured and retrieved frequency-resolved optical gating (FROG) traces for Yb: KGW-laser pulses compressed through filamentation under the conditions specified here are presented in Ref. [17]. The temporal envelope and the spectrum of the filamentation-compressed IR OPCPA pulse retrieved from such measurements are presented by circles in Figs. 5(a) and 5(b). As can be seen from the comparison of experimental results with simulations, the model adequately reproduces the

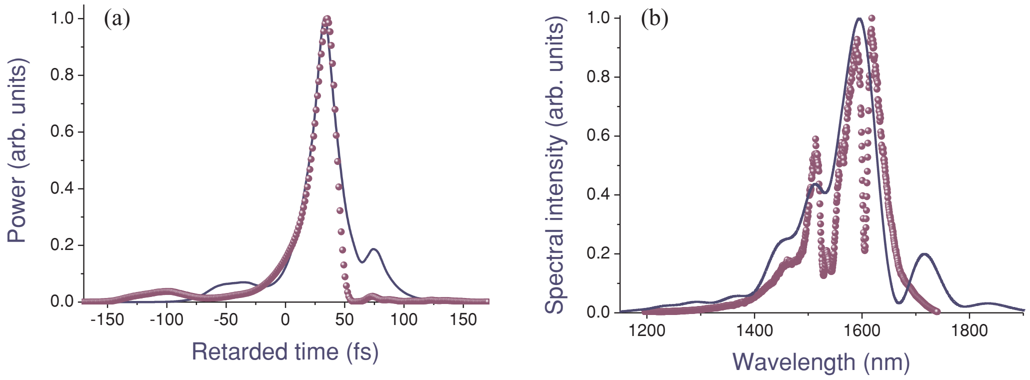

FIG. 5. (Color online) (a) Temporal envelope of the filamentation-compressed IR OPCPA pulse (circles) and temporal profile of the simulated field intensity integrated over the beam (solid line). (b) The spectra of the IR OPCPA pulse behind the filament: (circles) experiment, (solid line) simulations. The input pulse parameters and gas pressure are as specified in Fig. 1.

main features in the measured spectra and temporal pulse profiles. While the model predicts compression to an FWHM pulse width of 23 fs behind the filament, the temporal pulse envelope retrieved from the experimental data has an FWHM width of ~20 fs. In both experiments and theory, compressed laser pulses carry an energy of 1.5 mJ, which corresponds to an input-to-compressed-output energy conversion efficiency of ~70%. The leading edge of the pulse is only partially absorbed by the plasma of the filament, giving rise to a prepulse, seen near $\eta \approx -60$ fs in the map of Fig. 4(c), which translates into a prepulse of the compressed pulse behind the filament [see Fig. 5(a)]. The peak to the prepulse contrast ratio of the compressed pulse right behind the filament is ~15 in simulations [the solid line in Fig. 5(a)] and is estimated as 18 from the experimental results [circles in Fig. 5(a)]. The pulse continues to reshape as a part of its spatiotemporal dynamics also beyond $z = 145$ cm. However, the pulse remains shorter than 24 fs up to the point $z \approx 150$ cm and shorter than 30 fs up to $z \approx 170$ cm. Both in experiments and simulations, the beam remained stable as it propagated beyond the point of optimal compression.

The center of gravity of the spectrum, defined as $\lambda_{cg} = 2\pi c/\omega_{cg}$, where $\omega_{cg} = \int_{-\infty}^{\infty} \omega|A(\omega,r,z)|^2 d\omega[\int_{-\infty}^{\infty}|A(\omega,r,z)|^2 d\omega]^{-1}$, is located at 1.56 μm for the experimental spectra and at 1.54 μm for the simulated spectra. Defining the bandwidth of the laser pulse as $\Delta\omega = 2\sigma$, where $\sigma^2 = \int_{-\infty}^{\infty}(\omega - \omega_{cg})^2|A(\omega,r,z)|^2 d\omega[\int_{-\infty}^{\infty}|A(\omega,r,z)|^2 d\omega]^{-1}$, we find $\Delta\omega = 0.13$ PHz for the experimental spectrum and $\Delta\omega = 0.16$ PHz for its simulated counterpart. The discrepancy between simulations and experiments with regard to the local peak, appearing at 1720 nm in the simulated spectra [cf. the circles and the solid line in Fig. 5(b)], may be attributed to the long-wavelength limitation on the range of reliable spectral measurements imposed by the IR detector used in experiments. The validity range of the spectra retrieved from FROG measurements, on the other hand, extends beyond this point, suggesting that the local peak at 1720 nm may be physically meaningful. Although the simulations presented here have been intended to explain the results of experiments performed with 1.57-μm femtosecond laser pulses in argon at a pressure of 5 bars, the pulse compression scenario examined in this paper can also be implemented with other wavelengths and gas pressures.

We have demonstrated in this work that off-axial beam dynamics of ultrashort laser pulses in a filament enable a radical energy-throughput improvement for filamentation-assisted pulse compression. We have identified physical mechanisms whereby a weakly diverging wave, produced on the trailing edge of the pulse, catches up with a strongly diverging component, arising in the central part of the pulse, allowing sub-100-fs millijoule infrared laser pulses to be compressed to 20–25-fs pulse widths with energy throughputs in excess of 70%. Theoretical predictions have been verified by experimental results on filamentation-assisted compression of 70-fs, 1.5-μm laser pulses in high-pressure argon. In combination with novel sources of high-peak-power ultrashort pulses of long-wavelength radiation, which should help to suppress multiple filamentation, the nonparaxial filamentation-assisted pulse compression technique demonstrated in this work suggests a promising route toward the generation of terawatt CEP-stable few- and single-cycle electromagnetic field wave forms.

This work has been partially supported by the Seventh European Framework Program, Russian Foundation for Basic Research (Project No. 09-02-91004) and the Austrian Science Fund (FWF). An access to the Lomonosov supercomputer granted by Moscow State University is gratefully acknowledged. O.D.M. acknowledges support from an FWF Lise-Meitner Fellowship, Project No. M1094-N14.

---

[1] A. Braun, G. Korn, X. Liu, D. Du, J. Squier, and G. Mourou, Opt. Lett. **20**, 73 (1995).

[2] L. Bergé, S. Skupin, R. Nuter, J. Kasparian, and J.-P. Wolf, Rep. Prog. Phys. **70**, 1633 (2007).

[3] A. Couairon and A. Mysyrowicz, Phys. Rep. **44**, 47 (2007).

[4] N. Aközbek, A. Iwasaki, A. Becker, M. Scalora, S. L. Chin, and C. M. Bowden, Phys. Rev. Lett. **89**, 143901 (2002).

[5] A. Becker, N. Aközbek, K. Vijayalakshmi, E. Oral, C. M. Bowden, and S. L. Chin, Appl. Phys. B. **73**, 287 (2001).
[6] A. B. Fedotov, N. I. Koroteev, M. M. T. Loy, X. Xiao, and A. M. Zheltikov, Opt. Commun. **133**, 587 (1997).
[7] E. E. Serebryannikov, A. J. Verhoef, A. Mitrofanov, A. Baltuska, and A. M. Zheltikov, Phys. Rev. A **80**, 053809 (2009)
[8] M. Rodriguez, R. Bourayou, G. Méjean, J. Kasparian, J. Yu, E. Salmon, A. Scholz, B. Stecklum, J. Eislöffel, U. Laux, A. P. Hatzes, R. Sauerbrey, L. Wöste, and J.-P. Wolf, Phys. Rev. E **69**, 036607 (2004).
[9] J. Kasparian, M. Rodriguez, G. Méjean, J. Yu, E. Salmon, H. Wille, R. Bourayou, S. Frey, Y. B. Andre, A. Mysyrowicz, R. Sauerbrey, J. P. Wolf, and L. Woeste, Science **301**, 61 (2003).
[10] C. P. Hauri, W. Kornelis, F. W. Helbing, A. Heinrich, A. Couairon, A. Mysyrowicz, J. Biegert, and U. Keller, Appl. Phys. B **79**, 673 (2004).
[11] A. Couairon, J. Biegert, C. P. Hauri, W. Kornelis, F. W. Helbing, U. Keller, and A. Mysyrowicz, J. Mod. Opt. **53**, 87 (2006).
[12] A. Mysyrowicz, A. Couairon, and U. Keller, New J. Phys. **10**, 025023 (2008).
[13] E. Goulielmakis, S. Koehler, B. Reiter, M. Schultze, A. J. Verhoef, E. E. Serebryannikov, A. M. Zheltikov, and F. Krausz, Opt. Lett. **33**, 1407 (2008).
[14] F. Reiter, U. Graf, E. E. Serebryannikov, W. Schweinberger, M. Fiess, M. Schultze, A. M. Azzeer, R. Kienberger, F. Krausz, A. M. Zheltikov, and E. Goulielmakis, Phys. Rev. Lett. **105**, 243902 (2010).
[15] L. Bergé and S. Skupin, Opt. Lett. **33**, 750 (2008).
[16] T. Fuji, T. Suzuki, E. E. Serebryannikov, and A. M. Zheltikov, Phys. Rev. A **80**, 063822 (2009).
[17] O. D. Mücke, S. Ališauskas, A. J. Verhoef, A. Pugžlys, A. Baltuška, V. Smilgevičius, J. Pocius, L. Giniūnas, R. Danielius, and N. Forget, Opt. Lett. **34**, 2498 (2009).
[18] L. Bergé, Opt. Express **16**, 21529 (2008).
[19] A. A. Voronin, V .M. Gordienko, V. T. Platonenko, V. Ya. Panchenko, and A. M. Zheltikov, Opt. Lett. **35**, 3640 (2010).
[20] T. Brabec and F. Krausz, Phys. Rev. Lett. **78**, 3282 (1997).
[21] M. Geissler, G. Tempea, A. Scrinzi, M. Schnürer, F. Krausz, and T. Brabec, Phys. Rev. Lett. **83**, 2930 (1999).
[22] A. L. Gaeta, Phys. Rev. Lett. **84**, 3582 (2000).
[23] A. M. Perelomov, V. S. Popov, and M. V. Terent'ev, Zh. Eksp. Teor. Fiz. **50**, 1393 (1966) [Sov. Phys. JETP **23**, 924 (1966)].
[24] L. V. Keldysh, Zh. Eksp. Teor. Fiz. **47**, 1945 (1964) [Sov. Phys. JETP **20**, 1307 (1965)].
[25] H. J. Lehmeier, W. Leupacher, and A. Penzkofer, Opt. Commun. **56**, 67 (1985).
[26] A. Dalgarno and A. E. Kingston, Proc. R. Soc. London, Ser. A **259** 424 (1960).
[27] L. Bergé and S. Skupin, Phys. Rev. Lett. **100**, 113902 (2008).